

Cross-grating phase microscopy (CGM): *In-silico* experiments, noise and accuracy

BAPTISTE MARTHY¹ AND GUILLAUME BAFFOU^{1,*}

¹ Institut Fresnel, CNRS, Aix-Marseille University, Centrale Marseille, Marseille, France

* guillaume.baffou@fresnel.fr

Compiled March 15, 2022

Cross-grating phase microscopy (CGM) is a quantitative phase microscopy technique based on the association of a 2-dimensional diffraction grating (cross-grating) and a regular camera sensor, separated by a millimetric distance. This simple association enables the high-resolution imaging of the complex electric field amplitude of a light beam (intensity and phase) from a single image acquisition. While CGM has been used for metrology applications in cell biology and nanophotonics applications this last decade, there has been little study on its basics. In this article, we provide a numerical algorithm that enables the *in silico* data acquisition, to easily vary and observe the effects of all the CGM experimental parameters using computer means. In the frame of this article, we illustrate the interest of this numerical algorithm by using it to explain and quantify the effects of several important CGM parameters (grating-camera distance, pixel size, light intensity, numerical apertures, etc) on the noise, precision and trueness of CGM measurements. This work is aimed to push the limits of CGM toward advanced applications in biophysics and nanophotonics.

1. INTRODUCTION

Quantitative phase microscopy (QPM) refers to techniques capable of mapping the phase of a light beam [1–3] using optical microscopy means. Many different QPM techniques implemented on optical microscopes have been developed and improved these last two decades, namely digital holographic microscopy (DHM) [4, 5], spatial light interference microscopy (SLIM) [6, 7], diffraction phase microscopy (DPM) [8, 9], Shack-Hartmann wavefront sensing [10, 11] and quadriwave lateral shearing interferometry (QLSI) [12, 13]. QLSI is a QPM technique based on the association of a 2-dimensional diffraction grating (aka cross-grating) and a regular camera, separated by a millimetric distance (Figure 1a) [12]. This type of cross-grating phase microscopy (CGM), introduced and patented in 2000 by Primot [14, 15], has been used for the first time on a microscope in 2009, for bio-cell imaging and characterization [13, 16], and more recently in nanophotonics for the characterization of the optical properties of nanoparticles [17–19], 2D-materials [20] and metasurfaces [21] and as a temperature microscopy technique in nanoplasmonics [22–26]. Despite the gain of popularity of CGM, its basics remain poorly investigated in the field of optical microscopy.

In this article, we introduce an image processing algorithm that enables the simulation of experimental CGM images, taking into account the camera shot noise and light beam propagation between the cross-grating and the camera chip. Numerical results are compared with experimental measurements using a

home-made, tunable CGM set up to validate the algorithm. In a large part of the article, using this algorithm, we discuss the influence of parameters such as light wavelength, light intensity, grating-camera distance, relay lens magnification, numerical aperture (NA) of the illumination, on the image rms noise, measurement precision and trueness.

2. CROSS-GRATING PHASE MICROSCOPY (CGM)

A. Basic principle of CGM

Cross-grating phase microscopies (CGMs) use a 2D-dimensional diffraction grating (aka cross grating [27]) positioned at a millimetric distance from the chip of a regular camera [12]. Common cameras do not offer the possibility to place an object so close to the chip, due to presence of a sealed chamber. While some built-in commercial CGM systems exist, home-made systems rather involve a relay lens system that re-image the cross-grating at the desired distance from the camera chip (Figure 1a). The cross-grating creates a so-called interferogram image that is processed in real time to retrieve both the intensity and the phase of the incoming light beam. Unlike most QPMs, which directly measure and map the phase of light $\phi(x, y)$ by interferometry, CGM primarily measures the wavefront profile W of a light beam, or rather its gradients over the two directions of space (that are subsequently integrated). The interferogram consists of a dense array of bright spots, and the working principle resembles that of a Shack-Hartmann sensor [10, 11], although with a much higher spatial resolution. Then, the wavefront profile

W can be converted into the phase profile, if need be, using the relation

$$\phi(x, y) = \frac{2\pi}{\lambda} W(x, y), \quad (1)$$

where λ is the illumination wavelength. Thus, CGM is primarily a wavefront sensing technique that is commonly used as a phase microscopy technique.

CGM was not originally developed to be plugged onto an optical microscope. The original purpose of CGM was rather to characterize the quality of laser beams [28]. The idea to plug a CGM camera on a microscope to use it as a QPM for bioimaging dates from 2009 [13]. In this case, the wavefront profile results from a distortion due to the presence of a refractive object at the sample plane of the microscope, and is called the optical path difference (OPD) $\delta\ell = W$ (Figure 1b) and reads

$$\delta\ell(x, y) = (n - n_0) h(x, y) \quad (2)$$

where h is the thickness profile of the object, n the refractive index of the object and n_0 the refractive index of the environment.

Different types of cross-gratings have been used in CGM, with 3-fold or 4-fold symmetries [29], with different designs of the unit cell [30–33], or even with a thin (non-periodic) diffuser [34] or a binary random mask.[35] In the context of optical microscopy, the main instance of CGM that has been used so far is quadriwave lateral shearing interferometry (QLSI) [12, 13, 29]. QLSI cross-gratings feature a 4-fold symmetry consisting of horizontal and vertical opaque lines defining transparent squares imprinting 0 and π phase shifts on the incoming light according to a checkerboard pattern (Figure 1c).

B. CGM experimental set up

Although this article is mainly aiming at introducing a numerical algorithm, simulations will be compared with experimental measurements. To conduct these experiments, we used a home-made CGM set up, composed of a QLSI cross-grating, with a period of $\Lambda = 39 \mu\text{m}$ and a Sona camera from Andor. The grating was re-imaged using a relay lens (Fig. 1a) composed of two identical lenses (Thorlabs, TTL200-A, zoom $Z = 1$) and the grating-camera distance d was controlled using a stepper motor actuator (Thorlabs LNR25ZFS/M, KST101). The microscope was also home-made, composed of a $60\times$ objective lens (Olympus, LUCPLFLN60X) and a 180-mm tube lens (Thorlabs, TTL200-A). The sample was illuminated using a mounted LED at $625 \pm 25 \text{ nm}$ (Thorlabs, M625L3).

C. Experimental parameters in CGM

A CGM setup as depicted by Fig. 1a can be customized by varying several parameters, listed in Tab. 1, related to the features of the microscope, the grating and the camera. While commercial CGM systems are rather unchangeable, home-made CGM systems offer the possibility to vary and optimize the geometrical parameters (\mathcal{U} , Λ , d , β , Z) depending on the application and the sample. Optimizing experimentally the 11 parameters listed in Tab. 1 may be cumbersome, hence the interest of conducting *in-silico* experiments. Let us review and comment all the parameters of Table 1 one by one.

- λ_0 , $\Delta\lambda$. CGMs are achromatic. The knowledge of the illumination wavelength is not necessary to compute the wavefront profile from the interferogram, and varying the wavelength is not supposed to change the OPD profile retrieved from the interferogram. However, the phase shifts (0 and π in QLSI) are imprinted on the grating by etching the

substrate. Thus, the phase shifts are supposed to depend on the wavelength. However, if λ_0 deviates from the wavelength the grating has been made for, it is not supposed to lead biased measurement, but only poorer signal to noise ratio. Also, CGM does not require the use of coherent light sources (laser). On the contrary, it is even recommended to use temporally incoherent, broad band, light sources rather than a laser light to avoid the appearance of fringes on the intensity and phase images.

- w is the value of the brightest pixels of the interferogram (in photo-electrons). This value has to be adjusted just below the full well capacity of the camera chip to optimize the signal to noise ratio. In this article, we consider w to be the full well capacity. Typical scientific cameras feature a full well capacity ranging from 10000 to 50000, encoded in 16-bit.
- N_{im} is the number of averaged interferograms, or equivalently of OPD images (averaging one of the other type of images has an equivalent effect on the noise amplitude).
- p is the lateral size of the camera dixel. A dixel means 'detector element' [36], just like a pixel means a 'picture element'. We opt for this appellation instead of a camera pixel to avoid confusion with the pixel of an image.
- \mathcal{U} is the grating unit cell. Following the same logic, we shall call it a grexel (grating element). In this article, we focus on the cross grating used in QLSI, with a grexel characterized by a checkerboard pattern of 0 and π phase shifts. Importantly, the π phase shifts are imprinted on the grating by chemically etching the substrate by a specific depth L , so that $\pi = (n_{\text{subs}} - 1) L 2\pi / \lambda_0 \Rightarrow L \approx \lambda_0$, meaning that a QLSI grating is made for a particular wavelength. However, a variation of the nominal wavelength is supposed to mainly affect the signal to noise ratio, not the accuracy of the results. The grexel pattern of QLSI remained mostly unchanged for 20 years, except in a couple of articles. [30–33, 35]
- Λ and Z . Λ is the grexel lateral size, or equivalently the grating period. It is not a parameter that can be continuously modified experimentally, hence the interest of conducting *in silico* experiments. The relay lens magnification allows the artificial modification of the grating period Λ as seen by the camera, by a factor Z . The parameter that matters is thus the product ΛZ , i.e., the effective grexel size on the camera. An important feature of a CGM system, as explained later on, is the ratio ζ (zeta) between the effective grexel size ΛZ and the camera dixel size p :

$$\zeta = \frac{\Lambda Z}{2p}. \quad (3)$$

Common CGM cameras usually use $\Lambda = 6p$ or $8p$, i.e., $\zeta = 3$ or 4 . ζ must remain greater than 2.73 (Nyquist criterion) to enable proper imaging of the grexels, i.e., proper sampling of the fringes of the interferogram [13].

- d_{exp} is the distance between the grating and the image of the camera sensor created by the relay lens (see Fig. 1a).
- d is the effective grating-camera distance. It equals d_{exp} when the relay-lens has a magnification of $Z = 1$. But, when $Z \neq 1$, the displacement of the grating along z does not

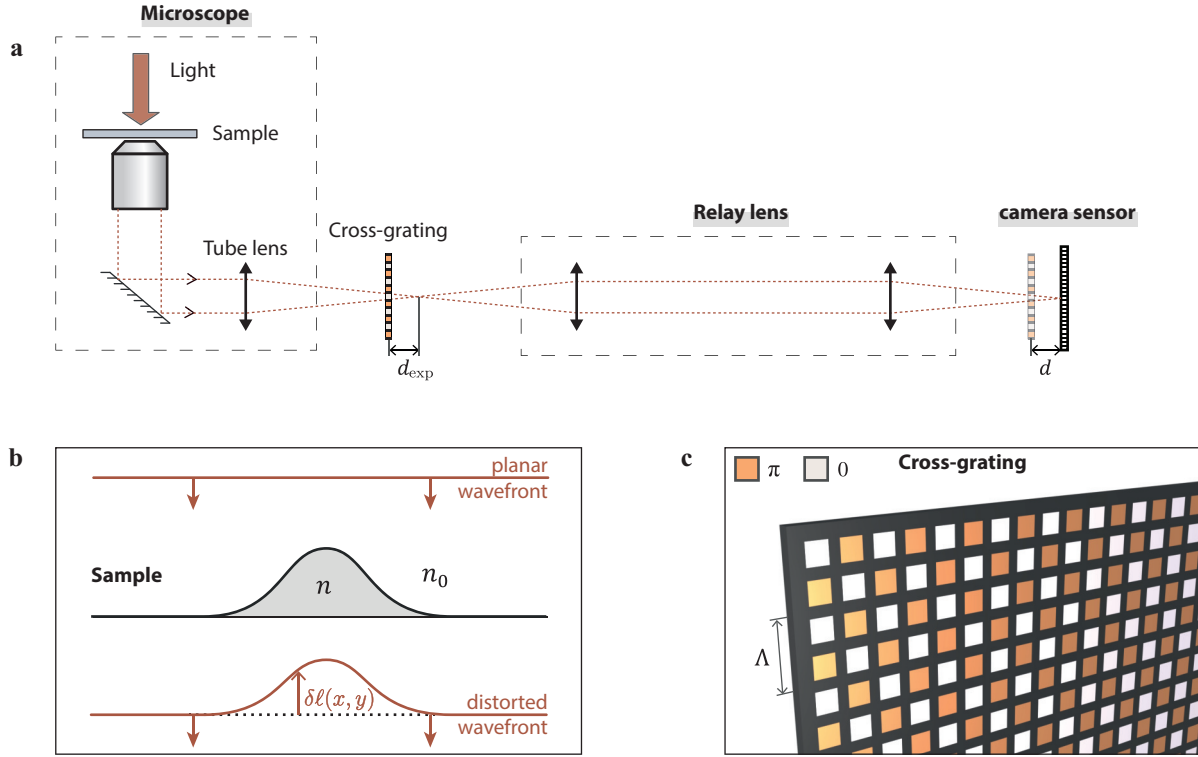


Fig. 1. Working principle of cross-grating microscopy. (a) Schematic of the experimental set up. (b) Optical wavefront distortion due to the presence of a transparent object, defining the optical path difference $\delta\ell$. (c) Representation of a QLSI cross-grating, characterized by a $0 - \pi$ checkerboard pattern.

Table 1. Definitions of the physical parameters involved in CGM, along with their particular values used in all the figures of this article.

Param.	Definition	Unit	Fig. 2&3	Fig. 4	Fig. 5	Fig. 6	Fig. 7
λ_0	Light central wavelength	nm	530	625	625	625	650
$\Delta\lambda$	Wavelength band width	nm	0	0	0	0	0
w	Maximum counts on the interferogram (full well capacity of the camera)		45000	40150	40000	40000	200
N_{im}	Number of averaged interferograms		5	30	25	25	1
p	Pixel size of the camera (dixel size)	μm	6.5	6.5	6.5	6.5	6.5
\mathcal{U}	Grating unit cell (grixel)	QLSI	QLSI	QLSI	QLSI	QLSI	QLSI
Λ	Grating period (grixel size)	μm	39	39	39	39, 52	52
Z	Zoom of the relay lens		1	1	1	1	1
d_{exp}, d	Grating-camera distance	mm	1	1.03	0.3 – 3	0.5 – 3	0.2 – 2.2
β	Grating tilt angle	deg	37°	37°	37°	37°	37°
NA_i	Numerical aperture of the illumination		0	0	0	0 – 0.9	0
N_x, N_y	Size of the OPD image	px	240	720	600	600	600
M	Magnification of the microscope					100	40

equal the one of its image. It is magnified by a factor of Z^2 as demonstrated in the appendix of Ref. [17]: $d = Z^2 d_{\text{exp}}$. d is an important parameter that affects both the precision and trueness of the measurements, as explained hereinafter. It usually lies in the millimetric range.

- β is the rotation of the grating around the optical axis. In practice, although CGM is supposed to normally work with $\beta = 0$, the cross-grating is usually tilted by an angle $\beta \neq 0$ around the optical axis to avoid Moiré effects and OPD reconstruction issues. For this reason, the algorithm we propose offers this option.
- NA_i is the NA of the illumination. It is an important parameter that can affect the signal to noise ratio of the reconstructed OPD image.
- (N_x, N_y) are the dimensions, in pixels, of the OPD image. These dimension are supposed to equal the ones of the interferogram, except for some algorithms that reduce the size of the OPD image to $(N_x/\zeta, N_y/\zeta)$, for the good of the speed for live imaging, but at the expense of the resolution of the image. In this article, we always process the OPD images so that they feature the same number of pixels as the interferogram, according to the algorithm we recently detailed in Ref. [12].
- M is the magnification of the microscope. It only matters when dealing with the illumination aperture or accuracy issues (see sections C and 5).

3. NUMERICAL PROCEDURE

Figure 2 depicts the algorithm we developed and introduce in this article to simulate experimental CGM images. We coin it the *insilex* (*in silico* experiment) algorithm. Here is a detailed description of it.

Figure 2a: First, the grexel pattern is designed. We focus in this article on a QLSI grexel, characterized by a $0-\pi$ checkerboard pattern. The aspect ratio of the dark lines width and the grexel size is $1/6$, a value aimed at optimizing the emission of light on the first orders of diffraction [15].

Figure 2b: The grexel should be tiled to form the full grating however. Prior to tiling, one can apply a tilt β of the grexel. A tilt by an arbitrary angle would produces discontinuities of the periodicity at the junction of the grexel tiles, upon tiling. To avoid this issue, we chose to tilt the grexel by a particular angle of $\beta = \cos^{-1}(4/5)$. This angle value ensures continuity if the unit-cell is made exactly 5 times bigger, leading to what we call the super unit-cell. This magic angle yield continuity upon tiling comes from the integer equality $3^2 + 4^2 = 5^2$.

Figure 2c: The grating super unit-cell is then resampled so that the pixel density matches the dixel density of the camera chip.

Figure 2d: Super unit-cells are tiled to get the complex transmittance T_g image of the full grating, of the size of the camera chip.

Figure 2e: The transmittance image T_g is multiplied by the electric field amplitude of the uniform incoming light beam, possibly tilted by a deviation angle ψ from the optical axis, and then propagated over a distance d to get the reference E -field on the camera. Considering a set of various illumination angles ψ enables the modelling of $\text{NA}_i \neq 0$.

Figure 2f,g: Meanwhile, intensity I_0 and phase ϕ_0 profiles are designed, corresponding to a desired object to be imaged. We

call them the *model* intensity and *model* phase images. Then, the scalar field $\sqrt{I_0} \exp(i\phi_0)$ is backward-propagated from the camera to the grating, multiplied by the grating transmittance T_g , and forward-propagated to get the E -field at the camera plane. Back and forth propagations are simulated using a standard Fourier-transform algorithm (see Matlab code `improp.m` in SI).

Figure 2h,i: The two interferograms are calculated from the two E -field maps, with and without the imaged object. Shot noise is added to the image. The amplitude of the shot noise is directly related to the number of counts on each dixel. In the *insilex* code, it is created using the `poissrnd` function of Matlab.

Figure 2j,k: Then, the home-made standard algorithm that we normally use to postprocess experimental interferograms is here applied to the simulated interferograms to retrieve the intensity I and phase ϕ images, to be compared with the model I_0 and phase ϕ_0 images. This algorithm consists in a demodulation of the image in the Fourier space to retrieve two wavefront gradients along orthogonal direction, which are then integrated to retrieve the wavefront profile (see Ref. [12] for details and the `CGMprocess.m` Matlab code in SI). Note that the postprocessing algorithm can also retrieve the intensity map from the interferogram by cropping the central spot in the Fourier space (not shown in Figure 2 for the sake of simplicity).

A Matlab package reproducing this algorithm is provided in Supplementary Material. As an initial test of the *insilex* algorithm, Fig. 3 plots the crosscut of the model OPD shown in Figure 2f (a simple Gaussian profile, 15 nm in amplitude), in comparison with a series of *in silico* calculated OPDs, where a proper agreement is observed. Such a good agreement is not always ensured. Further dispersion of the measurements (lack of precision) and measurement bias (trueness issue) can be encountered if the set of parameters listed in Table 1 is not properly adjusted. Next sections discuss these limitations to illustrate the interest of *in silico* experiments, and to eventually better define the best working area of CGMs, and QLSI in particular.

4. IMAGE NOISE AND PRECISION

Precision, trueness and accuracy are important to determine when conducting experimental measurement, and quantitative phase microscopy is no exception [16].

Precision refers to the standard deviation of an ensemble measurements performed in the same experimental conditions, for instance coming from the noise on the image. **Trueness** is the deviation of the measurements from the true value, also called a bias. **Accuracy**, sometimes mixed with the trueness, normally encompasses both precision and trueness. This section focuses on the estimation of the precision, while the next one focuses on the trueness.

A. White noise or Brown noise?

Figure 4 displays experimental and numerical flat OPD images (no object is imaged), as a means to highlight the image noise. Figure 4a shows an experimental OPD image (see Table 1 for details on the experimental conditions), along with its power spectral density (Fig. 4b). The noise in CGM mainly comes from the shot noise of the camera. Although a shot noise is a white noise (no spectral dependence on the spatial frequencies), OPD images in CGM do not feature a white noise, but rather a noise characterized by a $1/f^2$ power spectral density (Fig. 4b) where f represents the spatial frequencies of the image. A $1/f^2$ noise is usually called a Brown or Brownian noise. This particular noise arises from the integration step (Fig. 2k,l,m), not from

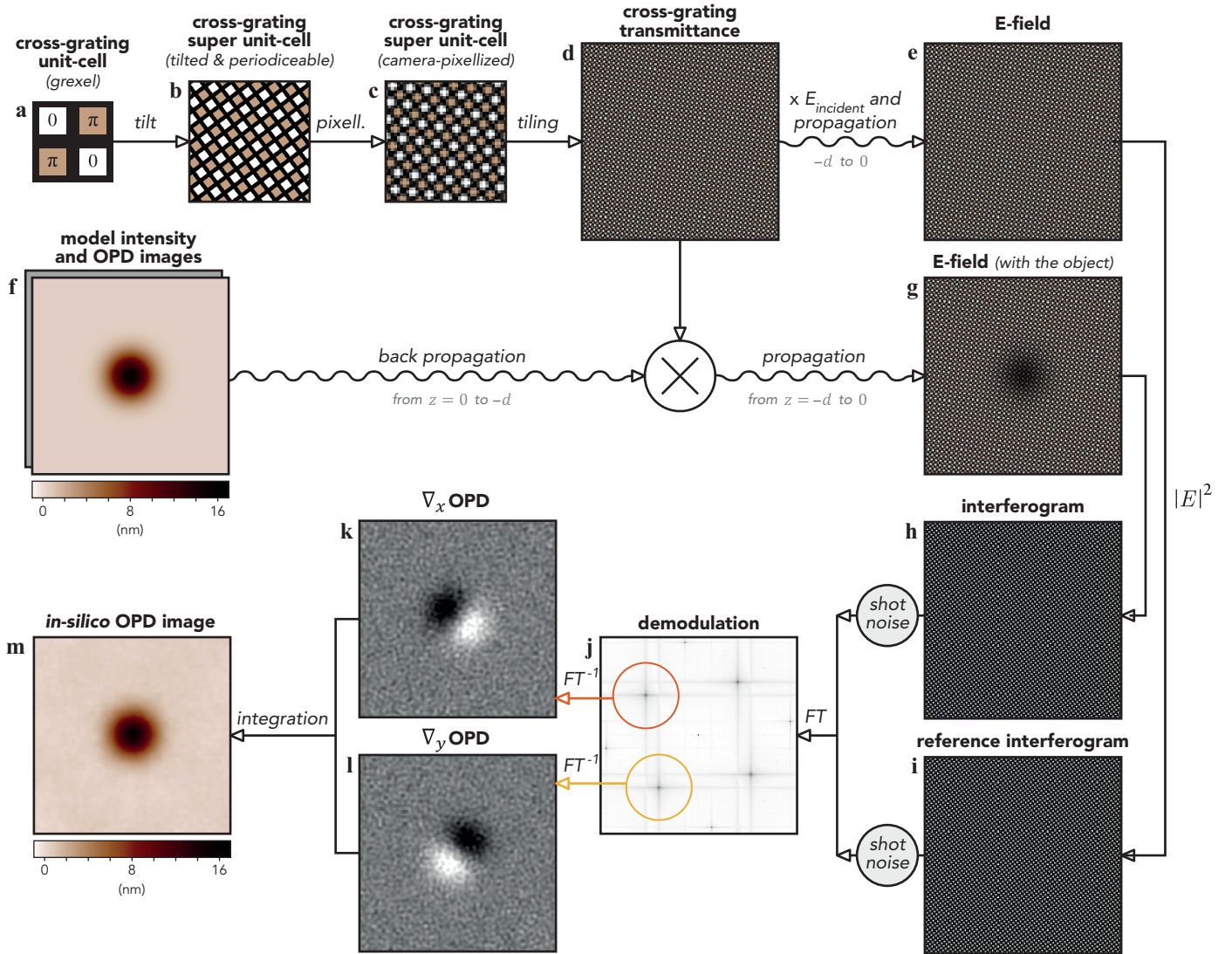


Fig. 2. Schematic of the algorithm for *in-silico* experiments (*insilex* algorithm). (a) Unit cell of the cross grating. Black lines are zero-transmission areas. (b) Tilt of the unit-cell by $\beta = \cos^{-1}(4/5)$ and enlargement by a factor of 5 to obtain a periodicable super unit-cell. (c) Pixelization of the super unit-cell according to the dixel size of the camera. (d) Tiling of the super unit-cell, up to the size of the camera chip. (e) Numerical propagation of the electric field from the grating to the camera chip. (f) Manually designed (model) OPD image $\delta\ell$ (here a Gaussian profile). (g) multiplication of the $\exp(i2\pi\delta\ell/\lambda_0)$ image by the cross grating transmittance. (h) Interferogram. (i) Reference interferogram followed by shot noise addition and 2D Fourier transform. (j) Demodulation of the interferograms. (k) Inverse Fourier transform and integration to obtain the *in silico* measured OPD, to be compared with (f).

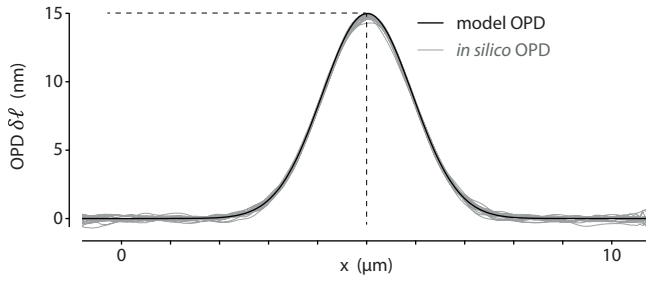


Fig. 3. Numerical simulation of the model OPD profile, and 17 experimental OPD profiles produced *in silico*.

the demodulation (Fig. 2j), as OPD gradients (Figure 2k,l) still feature a white noise. A Brown noise is indeed obtained by integrating a white noise.

Note the cutoff frequency at $f = N/6$, where $N \stackrel{\text{def}}{=} N_x = N_y$, in Fig. 4b. This cutoff comes from the demodulation step (Fig. 2j) that consists in cropping the Fourier space by a disc of diameter $N/(2\zeta)$.

Figure 4c displays an OPD image calculated using the *insilex* algorithm for the exact same parameters as Fig. 4a. This image along with its power spectral density plot (Fig. 4d) properly reproduce the experimental Brown nature of the noise (see Fig. 4a,b). As an illustration, a theoretically generated Brown noise is also shown in Figure 4e, which visually and spectrally exactly renders the same characteristics, expect that no cutoff frequency has been applied.

The noise standard deviation is slightly better (i.e. lower) in the *insilex* image, $\sigma_0 = 67$ pm, compared with the experimental image, $\sigma = 97$ pm. In CGM other sources of noise can be a setup misalignment, aberrations, sensor non-linearity, or a non-zero illumination NA (for the latter, see next section). Note that other types of camera noise, like read noise or thermal noise could also contribute. However, CGMs working conditions normally involve the full well capacity of the sensor, and short exposure times, so these other types of noise are supposed to be negligible. The read noise may become important if a large amount N_{im} images is averaged.

B. Noise estimation in CGM

The *insilex* algorithm enables the calculation of the fundamental, minimum noise standard deviation σ_0 that can be achieved in a CGM experiment as a function of all the experimental parameters. Measuring $\sigma > \sigma_0$ means that the setup can be further optimized. We conducted a large amount of *insilex* calculations, varying all the parameters, to understand all the dependencies of the parameters and derive a semi-empirical expression for σ_0 :

$$\sigma_0 = \frac{1}{8\sqrt{2}} \frac{pZ\Lambda}{d} \sqrt{\left(\frac{1}{N_{\text{im}}} + \frac{1}{N_{\text{im}}^0} \right) \frac{\log(N_x N_y)}{w}} \quad (4)$$

where N_{im} is the number of averaged interferograms, and N_{im}^0 is the number of averaged reference interferograms (equation coded in `sigma0.m`, in SI). Note that this expression considers a zero illumination NA ($\text{NA}_i = 0$). A refined expression of σ_0 including NA_i is given later (see Eq. Eq. (8)). One can also expression σ_0 at constant ζ parameter (ideally equal to 3), and

also considering the normal case where $N_{\text{im}} = N_{\text{im}}^0$:

$$\sigma_0 = \frac{p^2 \zeta}{4d} \sqrt{\frac{\log(N_x N_y)}{N_{\text{im}} w}} \quad (5)$$

This rearranged equation highlights the importance of the camera dixel size in CGM. In practice, the smaller the dixel size, the smaller the camera-grating distance has to be to avoid inaccuracies (see Eq. Eq. (9)), so that the ratio p/d must be kept constant, but still, this implies $\sigma_0 \sim p$, i.e., the smaller the dixel size, the better the signal to noise ratio.

Figure 5a,b plots *insilex* simulations of σ compared with σ_0 values given by Eq. Eq. (5), for $\zeta = 3, 4, 5$. A very good agreement is observed supporting the validity of Eq. Eq. (5). Figure 5c plots comparisons between σ_0 and experimental data, in the exact same conditions of parameters listed in Tab. 1. Experimental values are very close albeit slightly higher than the fundamental limit σ . As mentioned above, a higher noise level can have different origins. In our case, we suppose it can come from aberrations of the optics.

It is common to read attempts of noise and precision estimations in the literature in the context of QPM studies. Noise can be quantified in several manners. First, it can be calculated for a particular image and quantified by its standard deviation, as what we have done above. However, one may want to assign a noise level not to an image, but to a technique or a particular set up, as a means to compare different techniques with each other for instance. For this purpose, caution has to be used because noise levels obviously vary for a given setup, from one set of experimental conditions to another. In particular, noise standard deviation varies with light intensity \mathcal{I} and exposure time as $\sqrt{\mathcal{I}t}$. For this reason, as a means to get a more universal noise characterization taking into account the exposure time t dependence, noise amplitude is often given in $\text{nm}/\sqrt{\text{Hz}}$ units (for a signal in nm). However, this unit takes into account \sqrt{t} but not $\sqrt{\mathcal{I}}$. The quantity $\mathcal{I} \times t$ is nothing more than the density of light energy collected by the camera. This quantity is proportional to the number of photon collected per dixel. For this reason, as a more universal figure of merit, we propose here to define the noise of CGM as the noise standard deviation of a full-frame image when the camera sensor collects 40000 photons in the brightest pixels of the interferogram. This value roughly corresponds to the full well capacity of common scientific cameras. Thus, this definition gives an idea of the noise amplitude on OPD images arising from a single interferogram acquisition. Equation Eq. (5) leads an estimation of this figure of merit, that is $\sigma = 0.4$ nm/frame. To compare with other values from the literature sometimes given in $\text{nm}/\sqrt{\text{Hz}}$, one can consider a frame rate of 25 Hz to derive a noise level of $\sigma = 0.08$ nm/ $\sqrt{\text{Hz}}$.

C. Effect of the illumination NA

So far, we considered a zero-NA illumination (plane wave, $\text{NA}_i = 0$), also referred as a spatially *coherent* illumination. When the NA of the illumination is increased, one usually states that spatial coherence of the light is decreased. The illumination NA has a notable effect on the OPD image in CGM. First, it enables a kind of sectioning in z by blurring the out-of-plane parts of the imaged object [37]. Second, increasing NA_i , just like increasing NA_{obj} , leads to a better spatial resolution, a property advantageously used in Ref. [38].

However, increasing NA_i also tends to blur the interferogram, and thus increase the noise amplitude of the image. Such an effect was investigated and explained by Bon et al. in Ref. [13]. In

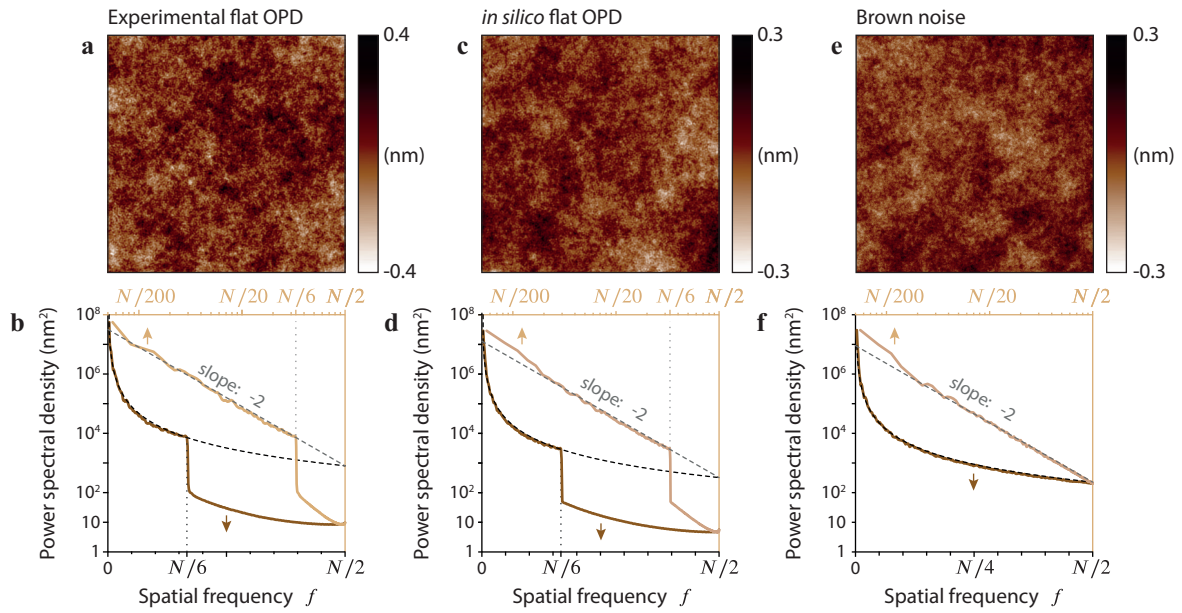


Fig. 4. Characterization of the image noise. (a) Experimental uniform OPD. (b) Spatial frequency spectrum of image (a). (c,d) Same as (a,b) for an *in silico* uniform OPD image in the same conditions. (e) Theoretical image featuring Brown noise. (f) Spatial frequency spectrum of the image (e).

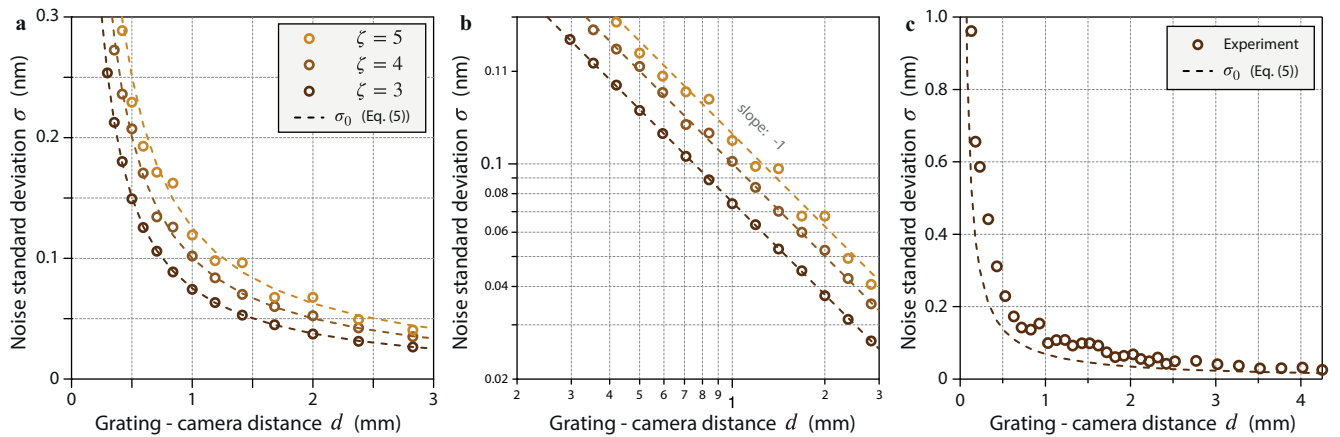


Fig. 5. Effect of the grating-camera distance on the image noise. (a) Noise standard deviation as a function of the grating-camera distance d for different values of the ζ parameter. Dashed lines represent σ values calculated using Eq. (5). (b) Same as (a) in logarithmic scale. (c) Experimental measurements of σ compared with the minimum noise standard deviation given by Eq. (5).

more detail, when a plane wave illuminates the sample with an incidence angle ψ , the transmitted plane wave through the optical microscope exhibits an incidence angle ψ_t on the camera sensor such that $\tan \psi_t = \tan \psi / M$, where M is the magnification of the microscope. This tilt angle ψ results in a translation of the interferogram in one direction by a distance $d \tan \psi_t = d \tan \psi / M$ (see the shadow picture in Ref. [12]). When a non-zero illumination NA is used, several illumination angles ψ enter into play and the final interferogram results from the incoherent sum of all the interferograms associated with all the illumination angles. Because they are all slightly shifted compared with each other on the camera plane, increasing the illumination NA results in a blurring of the interferogram, a lower contrast of the fringes and thus a higher noise on the OPD image. At some point, when NA_i reaches a critical values, the contrast is cancelled and the noise level diverges.[13]

The *in-silico* algorithm also offers the possibility to vary the illumination angle and, consequently, the illumination NA. A tilt angle can easily be applied during all the propagation steps (see Fig. 2) in the Fourier space. To model a given illumination NA, one just has to incoherently average all the interferograms corresponding to various illumination angles within the NA of the illumination, with a sufficient degree and discretisation.

Figure 6 plots the noise standard deviation σ of *insilex* OPD images as a function of the illumination NA NA_i , for various camera-grating distances d . For small values, NA_i does not affect the image and Eq. (5) giving the noise amplitude can be confidently used. However, for large NA, we observe the increase followed by a divergence of the noise amplitude, corresponding to a cancellation of the interferogram contrast. This cancellation and associated divergence occur for a very specific value of $NA_i = \psi_{i,max}$, as explained in Ref. [13], such that

$$KR = 1.22\pi \quad (6)$$

where $K = 4\pi/\Lambda$ and $R = d \tan \psi_{i,max}$. Results of Fig. 6 confirm exactly this condition. We indeed observe divergences of σ for NA_i values corresponding to Eq. (6) that we call the limiting NA NA_0 . In all the plots, the noise standard deviation σ could be nicely fitted with a function of the form $f(\zeta/d) = a_{fit}(\zeta/d) + b_{fit}(\zeta/d)/(NA_0(\zeta/d) - NA_i)$. We found an expression of the limiting NA

$$NA_0 = \sin \left[\tan^{-1} \left(\frac{1.22MZ\Lambda}{4d} \right) \right] \quad (7)$$

that exactly matches the condition Eq. (6) theoretically derived in Ref. [13]. Then, the values of a_{fit} and b_{fit} led us to the refined expression of σ_0 (refined Equation Eq. (5)) involving the illumination NA:

$$\sigma_0 = \left(\frac{pZ\Lambda}{8\sqrt{2}d} + \frac{NA_i}{NA_0 - NA_i} \times 3.54 \text{ [nm]} \right) \times \sqrt{\left(\frac{1}{N_{im}} + \frac{1}{N_{im}^0} \right) \frac{\log(N_x N_y)}{w}} \quad (8)$$

Figure 6 plots fits of all the *insilex* data using Eq. (8), showing an acceptable agreement.

5. TRUENESS

While the measurement precision is easy to measure, the trueness cannot always be quantified. Estimating the trueness of

a measurement requires the use of a calibrating sample. Interestingly, with the *insilex* algorithm, the trueness of CGM as a function of all the experimental parameters can be easily estimated, because the true OPD image is known (Fig. 2f).

Equation Eq. (5) suggests that the image noise can be infinitely dampen upon infinitely increasing the grating-camera separation d . As expected, this law holds true up to a certain limit. The limit is the accuracy. If the grating is put far away from the sensor, then the noise is reduced but the range of wavefront gradients that can be quantitatively imaged is also reduced. If the wavefront gradient is too steep, the integration algorithm yields incorrect reconstruction. As a consequence, although the noise can be infinitely reduced, one cannot infinitely increase the signal to noise ratio in CGM in a safe manner just by playing with the grating-camera distance.

To quantify this limitation, we ran *insilex* experiments on a model Gaussian OPD profile of amplitude A for a large range of d and Z values (grating-camera distance and magnification of the relay lens). Equivalently, Λ could have been spanned instead of Z because the effect of Z is to magnify the apparent size of the grixel on the camera sensor. For each set of d and Z parameters, a loop in A values (Figure 2f) was run until a discrepancy of 5% was observed between the actual A value and the one of the reconstructed OPD image (Figure 2m). This procedure enabled the phenomenological determination of the (d, Z) association of values that yield discrepancy. This set of values correspond to a limiting wavefront gradient on the camera that reads:

$$|\nabla_c W|_{\max} = \psi_{\max}^c = \frac{Z\Lambda}{4d} \quad (9)$$

∇_c means the gradient at the camera plane. Note that the gradient of the wavefront $\nabla_c W(x, y)$ is nothing but the local angle of incidence of the wavefront on the camera at (x, y) . Thus, equation Eq. (9) gives the expression of the maximum angle of incidence ψ_{\max}^c a wavefront can have on the camera to be properly characterized.

In practice, one rather deals with the wavefront profile at the sample plane, not at the camera plane. At the sample plane, the OPD amplitude remains unchanged, however, the wavefront is laterally shrinked and its gradient is thus magnified, by a factor of M , the magnification of the microscope. This condition yields the incidence angle threshold (IAT) at the sample plane:

$$|\nabla \delta \ell|_{\max} = \psi_{\max}^s = \frac{MZ\Lambda}{4d} \quad (10)$$

To better observe the nature of the problem that arises when the limit is reached, we conducted simulations at a specific $Z\Lambda$ value, and vary the distance d . Results are presented in Figure 7. The model object was a Gaussian OPD distribution (Figure 7a), impinging on the camera, $A = 3 \mu\text{m}$ in amplitude and 1.3 mm in full-width half-maximum (at the camera plane, so that the IAT is given by Eq. (9)). The OPD distribution is passed through the *insilex* algorithm to compute experimental images for different grating camera distances $d = 0.2, 1.4, 2.0, 2.2$ mm. The maximum counts on the camera has been set to a low value of $w = 200$ to highlight the effect of d on the noise. For $d = 0.2$ mm, a perfect agreement is found between model and *insilex* experiment, but a high noise level is also observed (Figs. 7d,e,f). In agreement with Eq. (5), this noise is reduced upon increasing d (Figs. 7g-o). However, at $d = 2.0$ mm, a small discrepancy is observed in the *insilex* Gaussian profile (Fig. 7k), an inaccuracy that becomes dramatic at $d = 2.2$ mm (Fig. 7n). This last example corresponds to the case where the wavefront profile locally exceeds the IAT

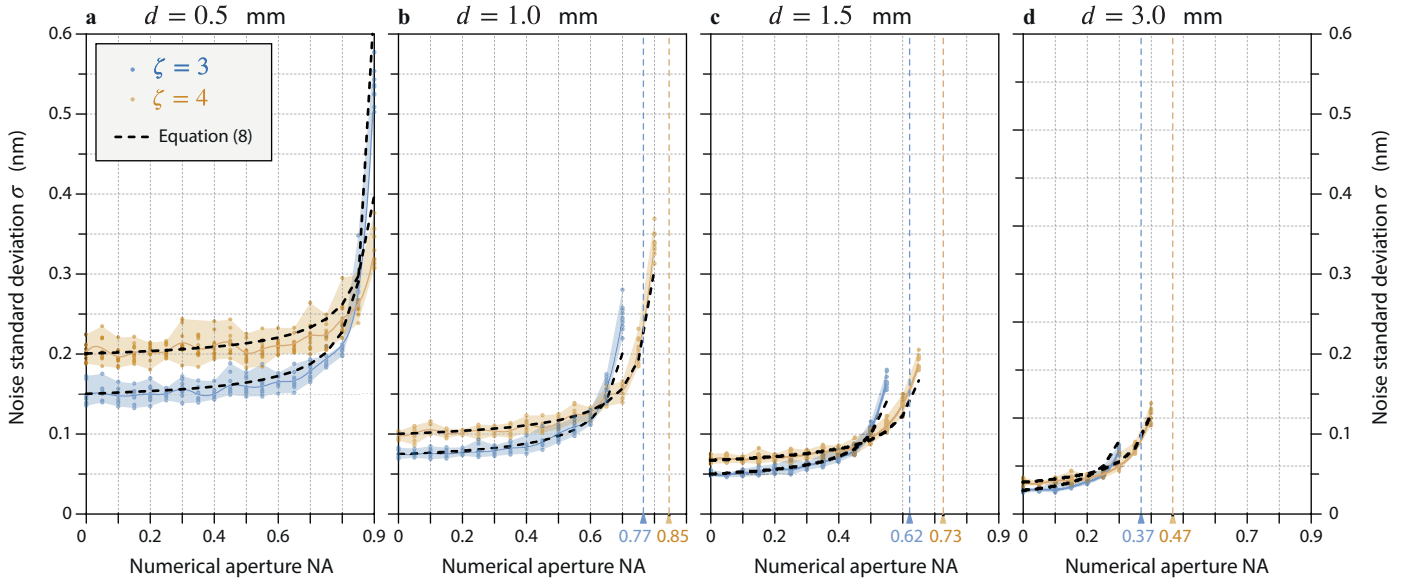


Fig. 6. Effect of the illumination numerical aperture on the image noise. Standard deviation of the noise as a function of the numerical aperture for grating-camera distances (a) $d = 0.5$ mm, (b) $d = 1.0$ mm, (c) $d = 1.5$ mm, (d) $d = 3.0$ mm. Each dot represents one *in-silico* measurement. Colored areas span from the minimum to the minimum values. Dashed lines represent σ_0 values calculated using Equation Eq. (8). In (b,c,d), NA_0 values (Eq. Eq. (7)) are indicated by vertical dashed lines.

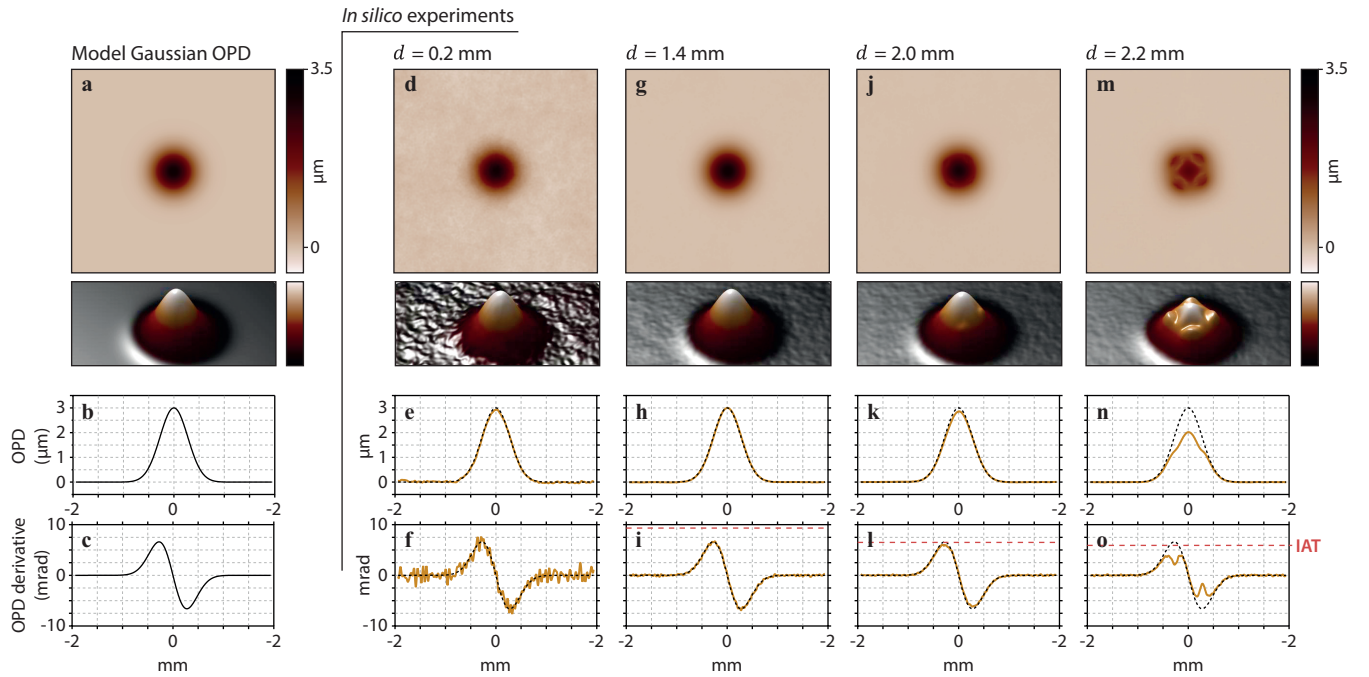


Fig. 7. Characterization of the accuracy. (a) Model Gaussian OPD distribution at the camera plane (3.9×3.9 mm² area), along with a 3D rendering of the image. (b) OPD cross-cut at the center of image (a). (c) Derivative of (b). (d,e,f) Same as (a,b,c) for an *in silico* experiment with a grating-camera distance of $d = 0.2$ mm. (g,h,i) Same as previously for a grating-camera distance of $d = 1.4$ mm. (j,k,l) Same as previously for a grating-camera distance of $d = 2.0$ mm. (m,n,o) Same as previously for a grating-camera distance of $d = 2.2$ mm. The dotted lines in (e,h,k,n) recall the model cross cut (b). The dotted lines in (f,i,l,o) recall the model derivative cross cut (c). The red dash lines in (i,l,o) indicate the incidence angle threshold (IAT) ψ_{\max} .

at some places in the image. Figures 7l,o plot the incidence angle (i.e., the derivative of the OPD at the camera plane) for the two problematic cases and we can see that the problem arises when the wavefront derivative reaches the IAT (dashed, red lines). When such an issue occurs experimentally, it usually leads to 4-fold symmetry artefacts (Fig. 7m), aligned with the grating tilt angle θ . Such an issue typically arises upon imaging objects with sharp boundaries. The effect is even stronger when the surrounding medium has a low refractive index (typically large dielectric beads in air). We personally encountered this issue when imaging micro-bubbles in liquids. To lift this problem, according to equation Eq. (10), either the grating has to be put closer to the camera, or the microscope magnification M has to be increased to expand the wavefront on the camera and diminish its gradient ψ^c .

6. SUMMARY AND PERSPECTIVE

In this article, we provide a numerical procedure to simulate experimental measurements in cross-grating phase microscopy (CGM). With such *in silico* experiments, it becomes possible to vary all the parameters involved in CGM experiments, including those that can hardly be varied in practice (or even cannot, with built-in systems), such as the camera-grating distance, grating pattern, camera pixel size, grating period, zoom of the relay lens, grating angle, etc. Importantly, the algorithm takes into account the noise formation of the reconstructed OPD images, the main concern to conduct challenging CGM experiments, at the limit of the state of the art, for instance for application in nanophotonics, or in microbiology where the objects of interest can be very thin, small and below the diffraction limit. The algorithm can help saving a considerable amount time and data storage space, by varying many parameters within numerical loops, instead of running actual experiments for months, in order to guide the adjustment of a CGM setup and the effective realization of actual experiments.

To illustrate the interest of the algorithm, we applied it to deepen the understanding of noise formation in CGM, and its implication in terms of precision and trueness. In particular, we derived fundamental expressions of the noise standard deviation and of the wavefront gradient limit, as a function of all the CGM parameters. However, the possibilities of this algorithm go much beyond. For instance, few investigations have been made in the improvement of the grating pattern, which has remained identical for 20 years (QLSI grating), especially because it would imply the expensive fabrication of a large amount of cross-gratings, and the associated masks for photolithography. We focused here on this popular QLSI pattern, but with the *in-silex* algorithm, one just has to modify a matrix to investigate and quantify the interest of any new grating pattern. Also, because actual noise is reproduced, the algorithm could be a priori used to easily build an arbitrarily large library of images as the ground truth to train segmentation or denoising deep-learning algorithms.

7. ACKNOWLEDGEMENT

This project received funding from the European Research Council (ERC) under the European Union's Horizon 2020 Research and Innovation Programme (grant agreement no. 772725, project HiPhore). The authors acknowledge support for the SATT Sud-Est.

8. BIBLIOGRAPHY

REFERENCES

1. M. Mir, R. Bhaduri, R. Wang, R. Zhu, and G. Popescu. Quantitative phase imaging. *Prog. Opt.*, 57:133–217, 2012.
2. T. Cacace, V. Bianco, and P. Ferraro. Quantitative phase imaging trends in biomedical applications. *Opt. Lasers Eng.*, 135:106188, 2020.
3. Y. K. Park, C. Depeursinge, and G. Popescu. Quantitative phase imaging in biomedicine. *Nat. Photonics*, 12:578–589, 2018.
4. E. Cuche, P. Marquet, and C. Depeursinge. Simultaneous amplitude-contrast and quantitative phase-contrast microscopy by numerical reconstruction of fresnel off-axis holograms. *Appl. Opt.*, 38(34):6994–7001, 1999.
5. P. Marquet, B. Rappaz, P. J. Magistretti, E. Cuche, Y. Emery, T. Colomb, and C. Depeursinge. Digital holographic microscopy: a noninvasive contrast imaging technique allowing quantitative visualization of living cells with subwavelength axial accuracy. *Opt. Lett.*, 30(5):468–470, 2005.
6. Z. Wang, L. Millet, M. Mustafa, H. Ding, S. Unarunotai, J. Rogers, M. U. Gillette, and G. Popescu. Spatial light interference microscopy (slim). *Opt Express*, 19(2):1016–1026, 2011.
7. X. Chen, M. E. Kandel, and G. Popescu. Spatial light interference microscopy: principle and applications to biomedicine. *Adv. Opt. Photon.*, 13(2):353–425, 2021.
8. B. Bhaduri, C. Edwards, H. Pham, R. Zhou, T. H. Nguyen, L. L. Goddard, and G. Popescu. Diffraction phase microscopy: principles and applications in materials and life sciences. *Adv. Opt. Photon.*, 6:57–119, 2014.
9. B. Kemper and G. von Bally. Digital holographic microscopy for live cell applications and technical inspection. *Appl. Opt.*, 47:A52–A61, 2008.
10. H. Gong, T. E. Agbana, P. Pozzi, O. Soloviev, M. Verhaegen, and G. Vdovin. Optical path difference microscopy with a shack–hartmann wavefront sensor. *Opt. Lett.*, 42:2122–2125, 2017.
11. J. Primot. Theoretical description of shack–hartmann wave-front sensor. *Opt. Commun.*, 222:81–92, 2003.
12. G. Baffou. Quantitative phase microscopy using quadriwave lateral shearing interferometry (qlsi): principle, terminology, algorithm and grating shadow description. *J. Phys. D: Appl. Phys.*, 54:294002, 2021.
13. Pierre Bon, Guillaume Maucort, Benoît Wattellier, and Serge Monneret. Quadriwave lateral shearing interferometry for quantitative phase microscopy of living cells. *Opt Express*, 17(15):13080–94, 2009. ISSN 1094-4087.
14. J. Primot. Three-wave lateral shearing interferometer. *Appl. Optics*, 32: 6242, 1993.
15. J. Primot and N Guérineau. Extended hartmann test based on the pseudoguiding property of a hartmann mask completed by a phase chessboard. *Appl. Opt.*, 39(31):5715–5720, 2000.
16. S. Aknoun, J. Savatier, P. Bon, F. Galland, L. Abdeladim, B. Wattellier, and S. Monneret. Living cell dry mass measurement using quantitative phase imaging with quadriwave lateral shearing interferometry: an accuracy and sensitivity discussion. *J. Biomed. Opt.*, 20(12):126009, 2015.
17. Samira Khadir, Patrick C. Chaumet, Guillaume Baffou, and Anne Sentenac. Quantitative model of the image of a radiating dipole through a microscope. *Journal of the Optical Society of America A*, 36(4):478–484, 2019. URL <http://josaa.osa.org/abstract.cfm?URI=josaa-36-4-478>.
18. S. Khadir, D. Andr n, P. C. Chaumet, S. Monneret, N. Bonod, M. K ll, A. Sentenac, and G. Baffou. Full optical characterization of single nanoparticles using quantitative phase imaging. *Optica*, 7:243–248, 2020.
19. P. Berto, E. Berm dez Ure a, P. Bon, R. Quidant, H. Rigneault, and G. Baffou. Quantitative absorption spectroscopy of nano-objects. *Phys. Rev. B*, 86:165417, 2012.
20. S. Khadir, P. Bon, D. Vignaud, E. Galopin, N. McEvoy, D. McCloskey, S. Monneret, and G. Baffou. Optical imaging and characterization of graphene and other 2d materials using quantitative phase microscopy. *ACS Photonics*, 4:3130–3139, 2017.

21. S. Khadir, D. Andr  n, R. Verre, Q. Song, S. Monneret, P. Genevet, M. K  ll, and G. Baffou. Metasurface optical characterization using quadriwave lateral shearing interferometry. *ACS Photonics*, 8:603–613, 2020.
22. G. Baffou, P. Bon, J. Savatier, J. Polleux, M. Zhu, M. Merlin, H. Rigneault, and S. Monneret. Thermal imaging of nanostructures by quantitative optical phase analysis. *ACS Nano*, 6:2452–2458, 2012.
23. G. Baffou, P. Berto, E. Berm  dez Ure  a, R. Quidant, S. Monneret, J. Polleux, and H. Rigneault. Photoinduced heating of nanoparticle arrays. *ACS Nano*, 7(8):6478–6488, 2013.
24. G. Baffou, E. Berm  dez Ure  a, P. Berto, S. Monneret, R. Quidant, and H. Rigneault. Deterministic temperature shaping using plasmonic nanoparticle assemblies. *Nanoscale*, 6:8984–8989, 2014.
25. H. M. L. Robert, J. Savatier, S. Vial, J. Verghese, B. Wattellier, H. Rigneault, S. Monneret, J. Polleux, and G. Baffou. Photothermal control of heat-shock protein expression at the single cell level. *Small*, 14:1801910, 2018.
26. S. Shakib, B. Rogez, S. Khadir, J. Polleux, A. W  rger, and G. Baffou. Microscale thermophoresis in liquids induced by plasmonic heating and characterized by phase and fluorescence microscopies. *J Phys Chem C*, 125(21533-21542), 2021.
27. M. Born and E. Wolf. *Principles of Optics: Electromagnetic Theory of Propagation, Interference and Diffraction of Light*. Cambridge University Press, 1999.
28. J. C. Chanteloup, F. Druon, M. Nantel, A. Maksimchuk, and G. Mourou. Single-shot wave-front measurements of high-intensity ultrashort laser pulses with a three-wave interferometer. *Opt. Lett.*, 23:621, 1998.
29. J. Primot and L. Sogno. Achromatic three-wave (or more) lateral shearing interferometer. *J. Opt. Soc. Am. A*, 12(12):2679, 1995.
30. C. Peng, F. Tang, X. Wang, and J. Li. Circular-aperture modified hartmann mask for quadriwave lateral shearing interferometry. *Opt. Commun.*, 451:86–96, 2019.
31. K. Patorski,   . S  luzewski, and M. Trusiak. 5-beam grating interferometry for extended phase gradient sensing. *Opt. Express*, 26:26872–26887, 2018.
32. Y. Li, J. Zhang, and J. Li. Generation and evolution of vortex array with variable-ratio lateral-shearing interferometry. *J. Opt.*, page accepted manuscript, 2022.
33. T. Ling, D. Liu, X. Yue, Y. Yang, Y. Shen, and J. Bai. Quadriwave lateral shearing interferometer based on a randomly encoded hybrid grating. *Opt. Lett.*, 40:2245, 2015.
34. P. Berto, H. Rigneault, and M. Guillon. Wavefront sensing with a thin diffuser. *Opt. Lett.*, 42:5117–5120, 2017.
35. C. Wang, Q. Fu, X. Dun, and W. Heidrich. Quantitative phase and intensity microscopy using snapshot white light wavefront sensing. *Sci. Rep.*, 9:13795, 2019.
36. Jerrold T. Bushberg. *The Essential Physics of Medical Imaging*. Lippincott Williams & Wilkins, 2011.
37. P. Bon, S. Aknoun, S. Monneret, and B. Wattellier. Enhanced 3d spatial resolution in quantitative phase microscopy using spatially incoherent illumination. *Optics Express*, 22:8654–8671, 2014.
38. P. Bon, S. L  cart, E. Fort, and S. L  v  que-Fort. Fast label-free cytoskeletal network imaging in living mammalian cells. *Biophys. J.*, 106:1588–1595, 2014.